Structure, shape and dynamics of biological membranes.

Idema, T.

CHAPTER 4

MEMBRANE SHAPES

In this chapter we study the shape of biomimetic ternary membranes. We find that in their ground state, vesicles which exhibit domains of two different phases fully phase-separate. The resulting shape is a trade-off between two competing effects: an elastic term, which wants the membrane to be as smooth as possible, and a boundary term, which wants to minimize the domain boundary length. The resulting minimal shape resembles a peanut or a snowman. We study the fluctuations of the membrane around this equilibrium shape. Moreover, we derive an analytical expression for the shape of the ground state. Fitting both the fluctuation spectrum and the equilibrium shape, we can extract the membrane's elastic (bending) modulus and the energy associated to the domain boundary (the line tension). The numbers we obtain can be used to give estimates and limits for the size and stability of nanodomains in the plasma membrane of living cells.

4.1 Introduction

In chapter 3 we studied the phase separation of biomimetic ternary membranes into liquid ordered (L_o) and liquid disordered (L_d) domains. Once phase separation starts, the domains have different physical parameters due to their unequal compositions. Moreover, a line tension associated to their boundaries emerges, as studied in section 3.4. The line tension contribution to the energy causes the domains to be circular in shape, minimizing their circumference for a given area. It also drives a coarsening process, since merging domains into larger ones reduces the total domain boundary length. Not surprisingly, the ground state is therefore a complete phase separation: a vesicle containing one L_o and one L_d domain.

There is an additional mechanism by which the line tension energy can be reduced: deformation of the vesicle. A uniform vesicle typically assumes a spherical shape, because that shape minimizes its bending energy (see section 2.3.5). If the total area and enclosed volume of the vesicle are fixed, it will always remain a sphere. However, over long timescales water can permeate the lipid bilayer membrane and the enclosed volume can be reduced. Using this degree of freedom, the energy associated with the line tension on the domain boundary can be reduced as well: by contracting the boundary, the vesicle can create a neck. If the line tension is large enough, the neck can be completely contracted and the vesicle can split in two, one part containing (mostly) a L_d membrane, the other a L_o one [6, 69, 82, 83]. The reason why this does not always happen is that this budding process is countered by the bending energy: the creation of the neck increases the total curvature of the vesicle. For moderate values of the line tension, the resulting stable shape therefore is a balance between the bending energy and the line tension energy, and resembles the 'snowman' of figure 2.1b. An example of an experimentally obtained picture of such a 'snowman' vesicle is shown in figure 4.1.

In this chapter we derive an analytical expression for the shape of a fully phase-separated vesicle. We verify the expression found by comparing it to the numerical shape obtained by minimizing the full energy functional. Moreover, we fit this model to experimental data to obtain numbers for the line tension τ and difference in Gaussian moduli of the phases $\Delta\bar{\kappa}$. Finally, we compare these numbers to existing models for living systems and use them to speculate on the existence and size of domains in the plasma membrane of cells.

The results reported in this chapter again apply to ternary vesicles, containing cholesterol, a low melting temperature lipid, and a high melting temperature lipid. In the experimental data presented here the low melting temperature lipid is DOPC and the high melting temperature lipid is (brain) sphingomyelin (SM). Alternatively, several other groups have used DPPC as the high melting temperature lipid and a great variety of low melting temperature lipids in their experiments, giving qualitatively similar results, see *e.g.* [2, 4–6, 54, 55, 79, 84–87]. Typically the L_o domains are rich in both sat-

urated tail lipids and cholesterol, whereas L_d domains are rich in lipids with unsaturated tails, see chapter 3.

The experimental data presented in this chapter was obtained by S. Semrau from the Leiden experimental biophysics group, and is used with permission. The experimental setup and procedure are briefly sketched in appendix 4.A; a more detailed overview can be found in [43].

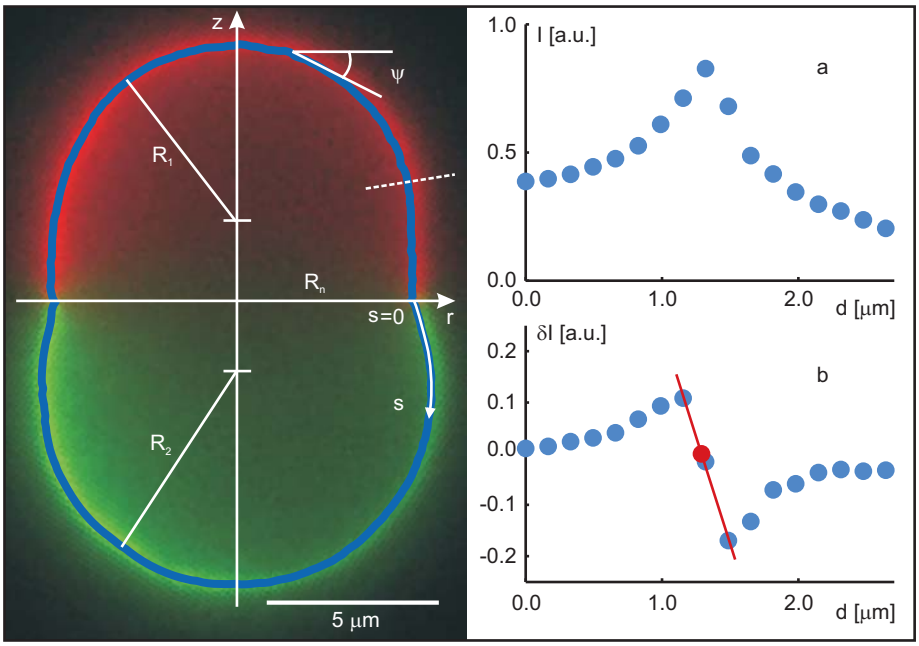

Figure 4.1: Equilibrium shape of a tricomponent vesicle which exhibits phase separation into a L_o and a L_d phase. The two phases have approximately equal surface area and the vesicle has been allowed to equilibrate for several weeks, allowing it to adjust its volume by transport of water molecules through the membrane. The resulting 'snowman' shape is the result of a balance between the bending energy and the line tension. The left figure shows the fluorescence raw data, with the L_o domain in red and the L_d domain in green; the contour is superimposed in blue. The insets on the right illustrate the principle of contour fitting. (a) Intensity profile normal to the vesicle contour (taken along the dashed line in the main image); (b) first derivative of the profile with linear fit around the vesicle edge (red line). The red point marks the vesicle edge.

4.2 Energy functional and shape equation

The free energy of the fully phase-separated vesicle with two domains (indicated by subscripts 1 and 2) is given by equation (2.102):

$$\mathcal{E} = \sum_{i=1}^{2} \int_{\mathcal{M}_i} \left(\frac{\kappa_i}{2}(2H)^2 + \bar{\kappa}_i K + \sigma_i \right) \mathrm{d}S + p \int \mathrm{d}V + \tau \oint_{\partial\mathcal{M}} \mathrm{d}l. \tag{4.1}$$

where the κ_i and $\bar{\kappa}_i$ are the bending and Gaussian moduli of the two domains, respectively, the σ_i are their surface tensions, τ is the line tension on their boundary and p is the pressure difference across the membrane. In the equilibrated shapes considered here, the force of the internal Laplace pressure is compensated by the surface tensions; consequently, both contributions drop out of the shape equations [48, 51]. As was shown in section 2.3.4, the Gauss-Bonnet Theorem allows us to integrate the Gaussian curvature term to a constant contribution on the bulk of each domain plus a boundary term. Within the bulk of each domain, the only relevant contribution to the energy is therefore giving by the bending term. Exploiting the fact that the vesicle is axisymmetric, and using the same notation as in section 2.3.5, we find that the shape of each bulk part is given by the following differential equation:

$$\ddot{\psi}\cos\psi = -\frac{1}{2}\dot{\psi}^2 \sin\psi - \frac{\cos^2\psi}{r}\dot{\psi} + \frac{\cos^2\psi + 1}{2r^2}\sin\psi. \tag{4.2}$$

where $\psi(s)$ is the tangent angle to the membrane, s the arc length measured along the vesicle contour and dots denote derivatives with respect to the arc length (see figure 2.1b). The vesicle's coordinates $r(s)$ and $z(s)$ are related to the tangent angle via the geometrical relations given by equations (2.88) and (2.89):

$$\dot{r} = \frac{\mathrm{d}r}{\mathrm{d}s} = \cos\psi(s), \tag{4.3}$$

$$\dot{z} = \frac{\mathrm{d}z}{\mathrm{d}s} = -\sin\psi(s). \tag{4.4}$$

We put the boundary between the two domains at $z = 0$ and also define $s = 0$ at this point. Of course r and ψ must be continuous at the boundary. As we derived in section 2.3.5, the variational derivation of equation (4.2) gives two more boundary conditions on $\dot{\psi}$ and $\ddot{\psi}$ [52]:

$$\lim_{\varepsilon\downarrow 0}(\kappa_2\dot{\psi}(\varepsilon) - \kappa_1\dot{\psi}(-\varepsilon)) = -(\Delta\kappa + \Delta\bar{\kappa})\frac{\sin\psi_0}{r_0}, \tag{4.5}$$

$$\lim_{\varepsilon\downarrow 0}\left(\kappa_2\ddot{\psi}(\varepsilon) - \kappa_1\ddot{\psi}(-\varepsilon)\right) = \left(2\Delta\kappa + \Delta\bar{\kappa}\right)\frac{\cos\psi_0\sin\psi_0}{r_0^2} + \frac{\sin\psi_0}{r_0}\tau, \tag{4.6}$$

where $\Delta\kappa = \kappa_2 - \kappa_1$, $\Delta\bar{\kappa} = \bar{\kappa}_2 - \bar{\kappa}_1$, and $r_0 = r(0)$ and $\psi_0 = \psi(0)$, are the radial coordinate and contact angle at the domain boundary.

4.3 Neck and bulk solutions

Far away from the domain boundary, the influence of the line tension at the boundary on the membrane shape is small. We therefore expect the membrane bending term to dominate the shape in the bulk of each domain. The optimal solution is then the least curved one, which is a sphere. Indeed the sphere is a solution of equation (4.2), and in the experimental pictures we clearly see that around the poles of the vesicle (putting the domain boundary at the equator) the shape becomes approximately spherical. We can therefore use the sphere as a first ansatz for the shape far from the domain boundary. Expanding around this ansatz, we can find corrections to the spherical shape from the shape equation (4.2). Close to the domain boundary, this approach breaks down, as the shape around the boundary is determined by the line tension, through the boundary conditions (4.5) and (4.6). We therefore split each of the domains into a bulk and a neck regime, where respectively the bending energy and the line tension dominate the shape.

As before, we put the domain boundary at $s = 0$. We denote the total arc length of the top domain by s_b and that of the bottom domain by s_e. The arc length coordinate s therefore has negative values in the top domain and positive values in the bottom domain, and runs over $(-s_b, s_e)$. The boundaries between the neck and bulk regimes in both domains are located at $s = -s_1$ and $s = s_2$ and the radii of the asymptotically approached spheres in both domains are given by R_1 and R_2.

For the bulk domains, we perform an analysis of small perturbations in $\psi(s)$ from the spherical ansatz. Due to the fact that we use an angular coordinate, there is a singularity at the poles of the vesicle, which translates into a divergence in the perturbative correction term. This divergence is unphysical and purely a consequence of the choice of coordinates. We should therefore restrict the perturbation to a region in which our chosen coordinate system has no singularities. The easiest choice is to calculate the perturbation for the region from $\psi = \pi/2$ to the domain boundary for the top domain, and analogously for the bottom domain. The details of the derivation of the bulk solution are given in appendix 4.C, the resulting shape is given by:

$$\psi_{\text{bulk}}(s) = \begin{cases} \frac{s+s_b}{R_1} & -s_b \leq s \leq -s_b + \pi R_1/2 \\ \frac{s+s_b}{R_1} + \frac{A_1 R_1^2}{2}\delta\psi\left(\frac{s+s_b}{R_1}\right) & -s_b + \pi R_1/2 \leq s \leq -s_1 \\ \pi + \frac{s-s_e}{R_2} + \frac{A_2 R_2^2}{2}\delta\psi\left(\pi + \frac{s-s_e}{R_2}\right) & s_2 \leq s \leq s_e - \pi R_2/2 \\ \pi + \frac{s-s_e}{R_2} & s_e - \pi R_2/2 \leq s \leq s_e \end{cases} \tag{4.7}$$

with

$$\delta\psi(x) = \frac{1}{\sin(x)} + x\log\left(\tan\left(\frac{x}{2}\right)\right) + i\left[\mathrm{Li}_2\left(i\tan\left(\frac{x}{2}\right)\right) - \mathrm{Li}_2\left(-i\tan\left(\frac{x}{2}\right)\right)\right] - (1-2K), \quad (4.8)$$

where A_1 and A_2 are integration constants, K is Catalan's constant, with numerical value ~ 0.91596559, and $\mathrm{Li}_n(z)$ the polylogarithm or Jonquière's function, defined as

$$\mathrm{Li}_n(z) = \sum_{k=1}^{\infty} \frac{z^k}{k^n}, \quad (4.9)$$

for $z \in \mathbb{C}$. The term containing the two polylogarithms in (4.8) is real for our region of interest ($-\pi < x < \pi$).

Near the domain boundary, ψ must have a local extremum in each of the phases and we can expand it as

$$\psi_{\mathrm{neck}}(s) = \begin{cases} \psi_0^{(1)} + \dot{\psi}_0^{(1)} s + \frac{1}{2}\ddot{\psi}_0^{(1)} s^2 & -s_1 \le s \le 0 \\ \psi_0^{(2)} + \dot{\psi}_0^{(2)} s + \frac{1}{2}\ddot{\psi}_0^{(2)} s^2 & 0 \le s \le s_2 \end{cases} \quad (4.10)$$

Because of the local extremum, the expansion for ψ_{neck} should be at least to second order. Because the boundary condition on $\ddot{\psi}$ tells us that due to the presence of a line tension at the domain boundary, $\dot{\psi}$ will be discontinuous at that boundary, so we can not go beyond second order without putting in additional information. The Canham-Helfrich energy functional (4.1) used here does not give that information; in order to refine the model we would need to use an energy functional that goes to at least fourth (instead of second) order in the local curvature (see section 2.3.5). For the model presented here, an expansion to second order for ψ_{neck} is therefore the appropriate one to use.

At the boundaries $s = -s_1$ and $s = s_2$ between the bulk and neck regimes, their respective solutions (4.7) and (4.10) should match smoothly. That means that ψ, as well as $\dot{\psi}$ and $\ddot{\psi}$ must be continuous at these points. Because we find $r(s)$ by integrating $\cos\psi(s)$, continuity of $\psi(s)$ implies continuity of $r(s)$ and no additional conditions are imposed at the regime boundaries. At the domain boundary ($s = 0$), the solution needs to satisfy the boundary conditions (4.5) and (4.6), as well as continuity of $\psi(s)$. Finally, there is a boundary condition on $r(s)$, which is that it must vanish at either pole (at $s = -s_b$ and $s = s_e$) to produce a closed vesicle. Equivalently, we can set $r(-s_b) = r(s_e) = 0$ and find $r_0 = r(0)$ by integration over each domain, giving the condition that $r(s)$ must be continuous at the domain boundary. In total, we have 10 conditions for the 10 unknowns $\{A_i, s_i, \psi_0^{(i)}, \dot{\psi}_0^{(i)}, \ddot{\psi}_0^{(i)}\}_{i=1,2}$.

Combined, the neck and bulk components of ψ give a vesicle solution for specified values of the material parameters $\{\kappa_i, \Delta\bar{\kappa}, \tau\}$. This solution compares extremely well to numerically determined shapes (obtained using the

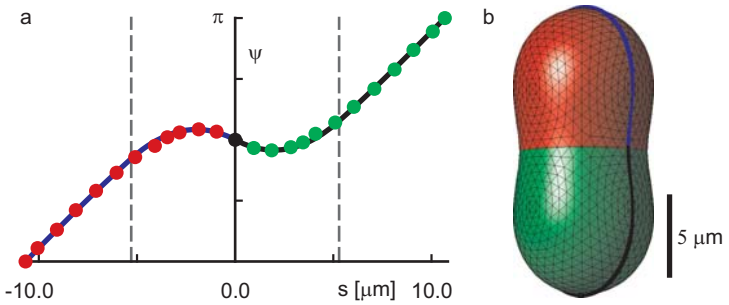

Figure 4.2: Numerically determined shape of a fully phase-separated vesicle with two domains of equal size. The shape was found by minimizing the free energy (4.1) by means of relaxation steps, using the software package Surface Evolver by Brakke [44]. The L_o phase is shown in red, the L_d phase in green. (a) Plot of contact angle ψ versus contour length s. The blue and black line shows the best fit of the model given by equations (4.7) and (4.10). The dashed lines mark the transition points between the neck and bulk regimes. (b) 3D representation of the entire vesicle. The optimal fit is again shown as a blue/black line.

Surface Evolver package [44], see figure 4.2). Moreover, for the symmetric case of domains with identical values of κ, we can compare to earlier modeling in Ref. [82]. The vesicle can then be described by a single dimensionless parameter $\lambda = R_0/\xi$, where $4\pi R_0^2$ equals the vesicle area, and $\xi = \kappa/\tau$ is known as the *invagination length*. The budding transition (where the broad neck destabilizes in favor of a small neck) is numerically found in Ref. [82] to occur at $\lambda = 4.5$ for equally sized domains; the model presented here gives a value of $\lambda = 4.63$.

4.4 Bending moduli and line tensions

The model for the shape of a fully phase-separated vesicle given by equations (4.7) and (4.10) has the bending moduli κ_i of the two domains, the line tension τ between them and the difference $\Delta\bar{\kappa}$ between their Gaussian moduli as input parameters. Moreover, the radii R_i of the two bulk spheres, and the sizes s_b and s_e of the domains, are also free parameters in the model and should be obtained from experiment. A direct fit of the model to an actual vesicle shape would therefore have many fit parameters and thus give unreliable results. Fortunately, the experimental data available provides us with more information than just the equilibrium shape of the vesicles. Using advanced detection techniques (see figure 4.1), it is possible to determine the membrane position

with an accuracy of $20\ \mathrm{nm}$, sufficient to determine the fluctuation spectrum, because thermal fluctuations occur on the scale of $50 - 100\ \mathrm{nm}$ [70]. From the vesicle shape we can directly obtain the radii and domain sizes. The bending moduli can subsequently be found from the fluctuation spectra, and the fit of the analytical model given by equations (4.7) and (4.10) finally gives the line tension and difference in Gaussian modulus.

We determined the bulk sphere radii R_i from the ensemble averaged radii of circles fitted to those parts of the contours that were nearly circular, *i.e.*, far away from the neck domain. We similarly found the domain sizes as the ensemble averaged total arc length of the equilibrium shape. We subsequently obtained spectra of the shape fluctuations for the nearly circular parts of the contour. We determined the fluctuations $u(s)$ for each single contour as the difference between the local radius r and the ensemble averaged radius R_i: $u(s) = r(s) - R_i$, with s again the arc length, see figure 4.3. Expanding fluctuations of the Canham-Helfrich free energy (2.78) in Fourier modes and invoking the Equipartition Theorem, we find an expression for the fluctuation spectrum in terms of the bending modulus κ and surface tension σ (see appendix 4.B). Taking into account the finite patch size [88] and following the spectral analysis of a closed vesicle shell developed by Pécréaux *et al.* [89], we find for the power spectrum for the vesicle fluctuation $u(s)$:

$$\overline{\langle |u_k|^2 \rangle} = \sum_{q_x} \left(\frac{\sin((k-q_x)\frac{a}{2})}{(k-q_x)\frac{a}{2}} \right)^2 \frac{k_{\mathrm{B}}T}{4\pi\eta L} \int_{-\infty}^{\infty} \mathrm{d}q_y \frac{\tau_q}{|\vec{q}|} \frac{\tau_q^2}{t^2} \left(\frac{t}{\tau_q} + e^{-t/\tau_q} - 1 \right). \tag{4.11}$$

Here $\vec{q} = (q_x, q_y) = \frac{2\pi}{L}(m,n)$ with m and n non-zero integers, $L = 2\pi R_i$, and η is the bulk viscosity of the surrounding medium. The overline indicates averaging over the illumination time, and the brackets denote the ensemble average. Fitting equation (4.11) to the measured fluctuation spectra (figure 4.3), we can extract the bending moduli and the surface tensions of both domains simultaneously. The numbers for five different vesicles of the same composition are listed in table 4.1. As can be seen from this table, the measured bending moduli $\kappa_{\mathrm{o}} = 8.0 \pm 0.7 \cdot 10^{-19}\ \mathrm{J} = 2.0 \pm 0.2 \cdot 10^2\, k_{\mathrm{B}}T$ and $\kappa_{\mathrm{d}} = 1.9 \pm 0.5 \cdot 10^{-19}\ \mathrm{J} = 50 \pm 13\, k_{\mathrm{B}}T$ of the L_{o} and L_{d} domains are the same for all five vesicles, confirming that these are a property of the membrane composition. In contrast, the values found for the surface tensions vary for the five vesicles measured, reflecting the fact that they depend on the exact preparation procedure and in particular the (small) pressure difference across the membrane. Using the values found from the fluctuation analysis, we have only two free parameters left in our model: the line tension τ and difference in Gaussian moduli $\Delta\bar{\kappa}$. We fitted the model given by equations (4.7) and (4.10) to the measured equilibrium shape in two ways to obtain the values of these parameters. The first method we used is a two-parameter fit, allowing the shape to optimize as a function of both parameters. The second method was to assume continuity of $\dot{\psi}$ across the domain boundary. This additional as-

sumption gives a direct relation between τ and $\Delta\bar{\kappa}$, leaving us with a single fit parameter. Both methods yield the same values for τ and $\Delta\bar{\kappa}$, which are listed in table 4.1 along with the bending moduli and surface tensions. As we would expect, the line tension depends on composition only, and for our specific choice has the value of 1.2 ± 0.3 pN, which is in the same range as that estimated by Baumgart *et al.* [6]. For the difference in Gaussian moduli we find $3 \pm 1 \cdot 10^{-19}$ J $= 8 \pm 3 \cdot 10^{1}\, k_B T$, in accordance with the earlier established upper bound ($\bar{\kappa} \leq -0.83\kappa$) reported by Siegel and Kozlov [90]. An example fit is given in figure 4.4.

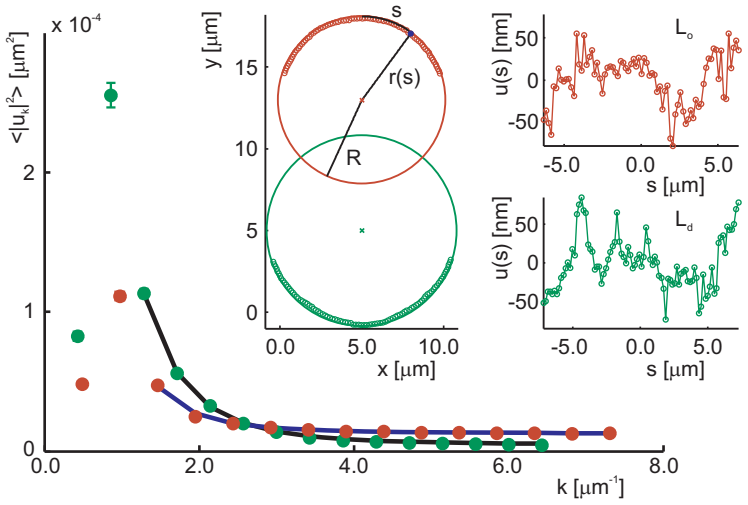

Figure 4.3: Fluctuation spectra of the ordered (red circles) and disordered (green circles) domains. The corresponding best fits of equation (4.11) are shown in blue and black respectively. Inset: Typical real-space fluctuations along the vesicle perimeter. Figure taken from [70].

4.5 Biological implications

Ultimately, we are interested in the membrane's elastic parameters because their precise magnitude has important consequences for the morphology and dynamics of cells. The literature is replete with theoretical speculations which depend strongly on, among others, the line tension. While the values we report apply to reconstituted vesicles, we can nonetheless use them in some of these models to explore possible implications for cellular membranes. The majority of the investigated vesicles finally evolved into the fully phase separated state. This finding is in agreement with previous work by Frolov *et al.* [91],

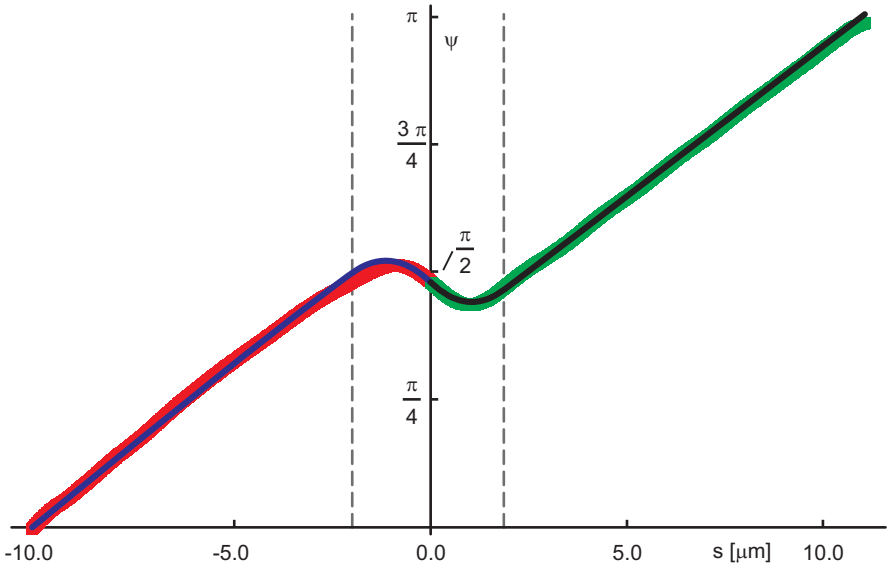

Figure 4.4: Example of an experimentally obtained $\psi(s)$ plot (red: L_o phase, green: L_d phase) together with the best fit of the model given by equations (4.7) and (4.10) in blue and black. The dashed lines mark the transition points between the neck and bulk regimes.

which predicts, for line tensions larger than $0.4\ \mathrm{pN}$, complete phase separation for systems in equilibrium. It should be noted that the line tension found is also smaller than the critical line tension leading to budding: recent results by Liu *et al.* [92] show that for endocytosis by means of membrane budding both high line tensions ($> 10\ \mathrm{pN}$) and large domains are necessary. Therefore nanodomains will be stable and will not bud off.

In cells, however, additional mechanisms must be considered. To explain the absence of large domains *in vivo*, Turner *et al.* [93] make use of a continuous membrane recycling mechanism. For the membrane parameters we have determined such a mechanism predicts asymptotic domains of $\sim 10\ \mathrm{nm}$ in diameter. Our results, in combination with active membrane recycling, therefore support a minimal physical mechanism as a stabilizer for nanodomains in cells. Domains continually nucleate and grow by coalescence, but are also continually removed from the (plasma) membrane by recycling processes.

A separate effect, purely based on the elastic properties of membranes may further stabilize smaller domains *in vivo*. Domains that are not flat within the environment of the surrounding membrane may interact via membrane deformations. Such interactions are studied in the next chapter.

	σ_{d} $(10^{-7}\,\mathrm{N/m})$	κ_{d} $(10^{-19}\,\mathrm{J})$	σ_{o} $(10^{-7}\,\mathrm{N/m})$	κ_{o} $(10^{-19}\,\mathrm{J})$	τ (pN)	$\Delta\bar{\kappa}$ $(10^{-19}\,\mathrm{J})$
1	2.8 ± 0.2	2.2 ± 0.1	0.3 ± 0.3	8.0 ± 1.3	1.5 ± 0.3	2.5 ± 2
2	5.8 ± 0.5	1.8 ± 0.2	2.1 ± 0.4	8.2 ± 1.5	1.2 ± 0.4	2.0 ± 2
3	3.5 ± 0.3	2.0 ± 0.1	2.0 ± 0.5	8.2 ± 1.4	1.2 ± 0.3	2.5 ± 2
4	2.8 ± 0.2	1.9 ± 0.1	2.5 ± 0.5	8.3 ± 1.2	1.2 ± 0.4	4.0 ± 2
5	2.3 ± 0.1	1.6 ± 0.1	0.6 ± 0.3	8.0 ± 1.6	1.1 ± 0.5	4.0 ± 3

Table 4.1: Values of the material parameters for five different vesicles. The surface tensions and bending moduli of the L_{d} and L_{o} phase are determined from the fluctuation spectrum; the line tension and difference in Gaussian moduli are subsequently determined using the analytical shape model given by equations (4.7) and (4.10).

4.A Experiments

The experimental data given in chapters 4, 5, and 6 were obtained by S. Semrau from the Leiden experimental biophysics group, and are used here with permission. In this appendix we briefly sketch the experimental procedure for obtaining the experimental data shown in figures 1.3, 4.1, 4.3, 4.4, 5.1, 5.2, 5.3, 5.6, 5.7, 5.8, 5.9 and 6.3. More details can be found in [43] and [71].

Giant unilamellar vesicles (GUVs) were produced from a mixture of $30\ \%$ DOPC, $50\ \%$ brain sphingomyelin, and $20\ \%$ cholesterol at $55°\mathrm{C}$. The L_{d} phase was stained by a small amount of Rhodamine-DOPE ($0.2\ \% - 0.4\ \%$), the L_{o} phase with a small amount ($0.2\ \% - 0.4\ \%$) of perylene. In the experimental results of chapter 4, the osmotic pressure on the inside and the outside of the GUVs was identical. In chapters 5 and 6, the partial budding of domains was stimulated by increasing the osmolarity on the outside of the vesicles by $40 - 50\ \mathrm{mM}$. In both cases, lowering the temperature to $20°\mathrm{C}$ resulted in the spontaneous nucleation of L_{o} domains in a L_{d} matrix. We observed that unbudded domains quickly merged to large ones, resulting in a vesicle exhibiting complete phase separation. An example of the raw data of such a vesicle is shown in figure 4.1. In contrast, partially budded domains posses long term stability (time scale of hours). A typical example of the dynamics of these domains is given in movie S1 of [71].

4.B Membrane fluctuations

In this appendix we use the Canham-Helfrich free energy functional (2.78) introduced in chapter 2 to derive the general expression for the fluctuations of a membrane patch based. We subsequently sketch how to obtain the expres-

sion for the fluctuation spectrum (4.11) of our phase-separated vesicle from this general expression. A detailed derivation of equation (4.11) can be found in [43, Chapter 2].

4.B.1 Fluctuations of a periodic membrane patch

From the Canham-Helfrich energy functional (2.78) introduced in chapter 2 it is a straightforward exercise to calculate the fluctuations of a flat piece of fluid membrane. This calculation is originally due to Helfrich [94] and can be found in detail in many textbooks, for instance Boal [95] or Chaikin and Lubensky [72]. We parametrize our flat piece of membrane using the Monge gauge introduced in section 2.3.1 and write $\vec{r} = (x, y, h(x, y))$, with $h(x, y)$ the height function in the z-coordinate. To lowest order in derivatives of h we can then calculate the mean curvature H and metric determinant $\det(g)$:

$$H = -\frac{1}{2}\nabla_\perp^2 h, \tag{4.12}$$

$$\det(g) = 1 + (\nabla_\perp h)^2, \tag{4.13}$$

where $\nabla_\perp$ denotes the two-dimensional gradient operator. Because we are only looking at fluctuations, the topology is constant and hence the contribution of the Gaussian curvature to the energy can be ignored. The energy of a membrane with surface tension σ and bending modulus κ to quadratic order in derivatives of h is then given by:

$$\mathcal{E} = \int_S \left(\frac{\kappa}{2}(2H)^2 + \sigma\right) \mathrm{d}A = \frac{1}{2}\int_S \left(\kappa(\nabla_\perp^2 h)^2 + \sigma(\nabla_\perp h)^2\right) \mathrm{d}x\,\mathrm{d}y. \tag{4.14}$$

We proceed by expanding h in Fourier modes, on a square piece of membrane of size $L \times L$ with periodic boundary conditions:

$$h(\vec{x}) = \sum_{\vec{q}} h_{\vec{q}}\, e^{i\vec{q}\cdot\vec{x}}, \tag{4.15}$$

where $\vec{x} = (x, y)$, $\vec{q} = (q_x, q_y) = \frac{2\pi}{L}(l_x, l_y)$ with $l_x, l_y \in \mathbb{Z}$, and

$$h_{\vec{q}} = \frac{1}{L^2}\int_{-L/2}^{L/2} \mathrm{d}x \int_{-L/2}^{L/2} \mathrm{d}y h(\vec{x}) e^{-i\vec{q}\cdot\vec{x}}. \tag{4.16}$$

Substitution of the Fourier expansion (4.15) in the expression (4.14) for the energy gives:

$$\mathcal{E} = \frac{L^2}{2}\sum_{\vec{q}} \left[\kappa(\vec{q}\cdot\vec{q})^2 + \sigma(\vec{q}\cdot\vec{q})\right] h_{\vec{q}} h_{\vec{q}}^*, \tag{4.17}$$

where the star denotes complex conjugation. Invoking the equipartition theorem we now immediately find for the static correlation function

$$\left\langle h_{\vec{q}} h^*_{\vec{q}} \right\rangle = \frac{1}{L^2} \frac{k_B T}{\kappa(\vec{q}\cdot\vec{q})^2 + \sigma(\vec{q}\cdot\vec{q})}, \tag{4.18}$$

where the brackets denote the ensemble average, k_B Boltzmann's constant and T the temperature.

4.B.2 Fluctuations of a membrane patch on a real vesicle

There are several differences between the actual situation when measuring membrane fluctuations on a real vesicle and the assumptions behind the calculation of the fluctuation spectrum (4.18). First, because with the microscope we observe an (optical) section of the membrane (the xz-plane, see figure 4.5), we cannot measure $h(x,y)$ but only $h(x,0)$.

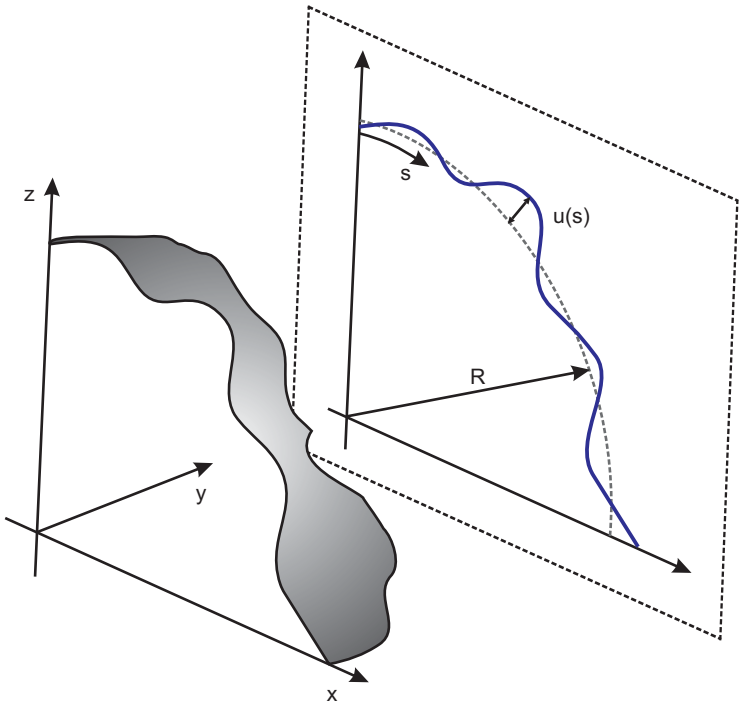

Figure 4.5: Optical section along the xz-plane, as measured in experimental observations of our vesicles. The ensemble-averaged radius is denoted by R, s is the contour length and $u(s)$ the deviation from R at s.

The Fourier components of the observable membrane profile $h(x,0)$ are given by

$$h_{q_x} = \frac{1}{L}\int_{-L/2}^{L/2} \mathrm{d}x h(x,0) e^{-iq_x\cdot x} = \sum_{q'_y} h_{(q_x,q'_y)}. \tag{4.19}$$

We can obtain the fluctuation spectrum of h_{q_x} from that of $h_{\vec{q}}$ if we convert the sum of equation (4.19) into an integral. A straightforward calculation gives:

$$\begin{aligned}\left\langle h_{q_x} h^*_{q_x}\right\rangle &= \frac{k_\mathrm{B}T}{2\pi L}\int_{-\infty}^{\infty}\mathrm{d}q_y \frac{1}{(q_x^2+q_y^2)((\sigma+\kappa q_x^2)+\kappa q_y^2)} \\ &= \frac{k_\mathrm{B}T}{2\sigma L}\left(\frac{1}{q_x} - \frac{1}{\sqrt{\frac{\sigma}{\kappa}+q_x^2}}\right).\end{aligned} \tag{4.20}$$

For tensionless membranes ($\sigma = 0$) or in the bending regime ($q_x^2 >> \sigma/\kappa$), the expression for the spectrum simplifies to

$$\left\langle h_{q_x} h^*_{q_x}\right\rangle = \frac{k_\mathrm{B}T}{4L}\frac{1}{\kappa q_x^3}. \tag{4.21}$$

The magnitude of short wavelength fluctuations thus only depends on the bending rigidity κ.

The model for the fluctuation spectrum of a flat membrane has to be adapted in two ways for the case of phase separated GUVs. We assume, as detailed above, that the vesicle is approximately spherical far away from the interface. As Pécréaux *et al.* [89] showed, for higher modes the fluctuation spectrum of a flat membrane with periodicity $L = 2\pi R$ is (numerically) the same as that of a sphere with radius R. Thus for fluctuations with short wavelengths (*i.e.*, higher modes) it does not matter that the membrane is curved on a length scale that is big compared to their wavelength. Therefore, we can in principle use the spectrum derived above, if we discard the lowest modes. However, the spherical part of the phase separated GUVs is not closed. Consequently, we have to derive the form of the spectrum for a finite membrane patch. Following [89] we choose $L = 2\pi R$ as the periodic interval and consider a patch of length a. For simplicity we choose a such that L is an integer multiple of a. We now denote the fluctuations of the contour with respect to the circle of radius R by $u(s)$, with s the arc length along the contour (see figure 4.5). Expanding $u(s)$ in Fourier modes, we have

$$u(s) = h(s,0) - R = \sum_k u_k e^{ik\cdot s}, \tag{4.22}$$

with $k = n\cdot\frac{2\pi}{a} = n\cdot m\cdot\frac{2\pi}{L}$, $n\in\mathbb{Z}$, $m\in\mathbb{N}$, and

$$u_k = \frac{1}{a}\int_{-a/2}^{a/2}\mathrm{d}s\, u(s) e^{-ik\cdot s}. \tag{4.23}$$

Following Mutz and Helfrich [88], we find for the spectrum of u_k:

$$\langle u_k u_k^* \rangle = \frac{k_B T}{2\sigma L} \sum_q \left(\frac{1}{q} - \frac{1}{\sqrt{\frac{\sigma}{\kappa} + q^2}} \right) \left[\frac{\sin\left((k-q)\frac{a}{2}\right)}{(k-q)\frac{a}{2}} \right]^2 . \tag{4.24}$$

The factor in square brackets in (4.24) goes to $\delta_{k,q}$ in the limit $a \to L$, so for $a = L$ we recover the fluctuation spectrum (4.18) of a closed sphere.

An experimental detail which further complicates the comparison of the calculated fluctuation spectrum with the experimental data, is that membrane contours are averaged over the camera integration time t (which equals the illumination time). Consequently, we observe time averaged fluctuations:

$$\overline{u(s)} = \frac{1}{t} \int_0^t \mathrm{d}t' u(s,t'). \tag{4.25}$$

To determine the influence of time averaging on the spectrum we need to know the correlation times of the fluctuation modes [89, 96]:

$$\left\langle h_{\vec{q}}(t_1) h_{\vec{q}}^*(t_2) \right\rangle = \left\langle h_{\vec{q}} h_{\vec{q}}^* \right\rangle \exp\left(-\frac{|t_1 - t_2|}{\tau_q} \right), \tag{4.26}$$

where τ_q is the correlation time, given by

$$\tau_q = \frac{4\eta|\vec{q}|}{\kappa(\vec{q}\cdot\vec{q})^2 + \sigma(\vec{q}\cdot\vec{q})}, \tag{4.27}$$

and η is the bulk viscosity of the medium surrounding the membrane. For the time-averaged spectrum we find

$$\begin{aligned} \overline{\left\langle h_{\vec{q}} h_{\vec{q}}^* \right\rangle} &= \frac{1}{t^2} \int_0^t \mathrm{d}t_1 \int_0^t \mathrm{d}t_2 \left\langle h_{\vec{q}}(t_1) h_{\vec{q}}^*(t_2) \right\rangle \\ &= \frac{k_B T}{2\eta|\vec{q}|L^2} \frac{\tau_q^3}{t^2} \left(\frac{t}{\tau_q} + e^{-t/\tau_q} - 1 \right). \end{aligned} \tag{4.28}$$

Combining equations (4.24) and (4.28), we find for the time averaged fluctuation spectrum of a finite membrane patch

$$\overline{\langle |u_k|^2 \rangle} = \sum_{q_x} \left(\frac{\sin((k-q_x)\frac{a}{2})}{(k-q_x)\frac{a}{2}} \right)^2 \frac{k_B T}{4\pi\eta L} \int_{-\infty}^{\infty} \mathrm{d}q_y \frac{\tau_q}{|\vec{q}|} \frac{\tau_q^2}{t^2} \left(\frac{t}{\tau_q} + e^{-t/\tau_q} - 1 \right). \tag{4.29}$$

4.C Finding the bulk solution

The shape of a vesicle of which the membrane is uniform in composition, and the volume is unconstrained, is given by the shape equation (4.2)

$$\ddot{\psi}\cos\psi = -\frac{1}{2}\dot{\psi}^2 \sin\psi - \frac{\cos^2\psi}{r}\dot{\psi} + \frac{\cos^2\psi + 1}{2r^2}\sin\psi. \tag{4.30}$$

If there are no boundary conditions, the solution of equation (4.30) is a sphere. Its tangent angle and radial coordinate are given by

$$\psi(s) = \frac{s}{R}, \tag{4.31}$$

$$r(s) = R\sin(\psi(s)) = R\sin\left(\frac{s}{R}\right), \tag{4.32}$$

where R is the radius of the sphere and s the arc length measured along the sphere. As explained in section 4.3, the sphere is a good approximation for those parts of a two-domain, 'snowman'-shaped vesicle which are far away from the domain boundary. However, the line tension associated with the domain boundary may cause deformations which carry into the bulk regime. To find the correct shape for the bulk part of the vesicle we should therefore allow for a perturbation of the spherical shape given by equations (4.31) and (4.32). We do so by adding a perturbation $\delta\psi$ to the tangent angle and write

$$\psi(s) = \frac{s}{R} + \delta\psi(s). \tag{4.33}$$

We assume $\delta\psi(s)$ to be small compared to ψ, and moreover, that the derivatives of $\delta\psi(s)$ with respect to s are also small, *i.e.*, of the same magnitude as $\delta\psi(s)$ itself. Because the shape equation (4.30) does not only contain derivatives of $\psi(s)$, but also its integral $r(s)$, we need to know how the perturbation affects $r(s)$ as well. To do so, we integrate the geometric relation given by (4.3): $\dot{r} = \cos\psi(s)$, and find:

$$\begin{aligned} r(s) &= R\sin(s/R) - \int_{s_0}^{s} \delta\psi(s')\sin(s'/R)\,\mathrm{d}s' + \mathcal{O}(\delta\psi^2) \\ &= R\sin(s/R) + R\Big[\delta\psi(s')\cos(s'/R)\Big]_{s'=s_0}^{s'=s} \\ &\qquad -R\int_{s_0}^{s} \delta\dot{\psi}(s')\cos(s'/R)\,\mathrm{d}s' + \mathcal{O}(\delta\psi^2) \\ &= R\sin(s/R) + R\cos(s/R)\delta\psi(s) \\ &\qquad -R\int_{s_0}^{s} \delta\dot{\psi}(s')\cos(s'/R)\,\mathrm{d}s' + \mathcal{O}(\delta\psi^2), \end{aligned} \tag{4.34}$$

where $\delta\dot{\psi}(s) = \mathrm{d}\psi(s)/\mathrm{d}s$ and s_0 is an appropriately chosen reference point. When going from the second to the third line in (4.34), we assumed $\delta\psi$ vanishes at s_0, which will set s_0 later on. Unfortunately, equation (4.34) can not be substituted directly in the shape equation (4.30) because of the integral expression. We therefore use another approach: we isolate $r(s)$ from (4.30), differentiate once with respect to s, and use (4.3) for $\dot{r}$. The resulting differential equation will give us an explicit expression for $\delta\dot{\psi}(s)$, which we can use in (4.34) to find the explicit dependence of $r(s)$ on $\delta\psi(s)$. Rewriting (4.30), and dropping

the explicit dependencies on s, we have

$$r^2(2\ddot{\psi}\cos\psi + \dot{\psi}^2\sin\psi) + r(2\cos^2\psi\dot{\psi}) - (\cos^2\psi + 1)\sin\psi = 0, \tag{4.35}$$

from which we get two solutions for $r(s)$:

$$r(s) = \frac{1}{2\ddot{\psi} + \dot{\psi}^2\tan\psi}\left(-\cos\psi\dot{\psi} \pm \sqrt{\dot{\psi}^2\sec^2\psi + 2\ddot{\psi}\tan\psi(1+\cos^2\psi)}\right). \tag{4.36}$$

We can differentiate both sides of (4.36) with respect to s. We then substitute (4.3), and expand of ψ as given in (4.31). When taking the plus sign in equation (4.36), this procedure gives:

$$\begin{aligned}
&\cos(s/R) - \sin(s/R)\delta\psi \\
&= R\frac{\mathrm{d}}{\mathrm{d}s}\Big[\sin(s/R) + \cos(s/R)\delta\psi - R\sin(s/R)\delta\dot{\psi} \\
&\qquad\qquad -R^2\sin^2(s/R)\cos(s/R)\delta\ddot{\psi}\Big] \\
&= \cos(s/R) - \sin(s/R)\delta\psi - 3R^2\sin(s/R)\cos^2(s/R)\delta\ddot{\psi} \\
&\qquad\qquad -R^3\sin^2(s/R)\cos(s/R)\delta\dddot{\psi}
\end{aligned} \tag{4.37}$$

so

$$0 = 3\cos(s/R)\delta\ddot{\psi} + R\sin(s/R)\delta\dddot{\psi}. \tag{4.38}$$

For the minus sign in (4.36), we find

$$\begin{aligned}
0 &= 2\frac{\sin(s/R)\cos(s/R)}{1+\cos^2(s/R)} - 2\sin(s/R)\delta\psi - R^2\cos^2(s/R)(4+3\sin^2(s/R))\delta\ddot{\psi} \\
&\qquad +R^3\sin(s/R)\cos(s/R)(1+\cos^2(s/R))\delta\dddot{\psi}.
\end{aligned} \tag{4.39}$$

Equation (4.39) we will not attempt to solve analytically; a numeric solution shows that the solution grows quickly and can not be considered a small perturbation to the sphere. Equation (4.38) can be integrated directly, resulting in an expression for $\delta\ddot{\psi}$:

$$\delta\ddot{\psi}(s) = A\csc^3\left(\frac{s}{R}\right), \tag{4.40}$$

with A an integration constant which has dimension $1/R^2$. Integrating again, we get

$$\delta\dot{\psi}(s) = \frac{AR}{2}\log\left[\tan\left(\frac{s}{2R}\right)\right] - \frac{AR}{2}\frac{\cos(s/R)}{\sin^2(s/R)} + b, \tag{4.41}$$

where b is another integration constant. Because the integral of b gives a term that scales with s, it gives a constant contribution to the term s/R in $\psi(s)$; we therefore set $b = 0$. A final integration gives us $\delta\psi(s)$:

$$\begin{aligned}
\delta\psi(s) &= \frac{AR^2}{2}\left[\frac{1}{\sin(s/R)} + \frac{s}{R}\log\left(\tan\left(\frac{s}{R}\right)\right)\right. \\
&\qquad \left. + i\left(\mathrm{Li}_2\left(i\tan\left(\frac{s}{2R}\right)\right) - \mathrm{Li}_2\left(-i\tan\left(\frac{s}{2R}\right)\right)\right)\right] + d,
\end{aligned} \tag{4.42}$$

with d another integration constant and $\mathrm{Li}_n(z)$ the polylogarithm (also known as Jonquière's function), defined as

$$\mathrm{Li}_n(z) = \sum_{k=1}^{\infty} \frac{z^k}{k^n}, \tag{4.43}$$

for $z \in \mathbb{C}$. The combination of the two polylogarithms in (4.42) is real for our region of interest ($-\pi R < s < \pi R$). We should choose d such that $\delta\psi(s_0) = 0$, which gives

$$d = -\frac{AR^2}{2}(1 - 2K) \tag{4.44}$$

where K is Catalan's constant, with numerical value ~ 0.91596559.

Having found expressions for $\delta\psi(s)$ and $\delta\dot{\psi}(s)$, we can use (4.34) to find $r(s)$. Using equation (4.41), the integral in (4.34) can be evaluated exactly:

$$\begin{aligned} r(s) \quad = \quad & R\sin(s/R) + R\cos(s/R)\delta\psi(s) \\ & -\frac{AR^3}{2}\left[\cot(s/R) + \log\left(\tan\left(\frac{s}{2R}\right)\right)\sin(s/R)\right]. \end{aligned} \tag{4.45}$$

Because we work with an angular coordinate, there is a coordinate singularity at the poles of the vesicle, causing a divergence in $\delta\psi(s)$. This divergence is unphysical, and can be avoided by choosing s_0 at any point away from the pole. The easiest choice is to take $\psi(s_0) = \pi/2$ (top domain), *i.e.*, at the equator of the domain, and analogously for the bottom domain. Continuity of $r(s)$, $\psi(s)$ and $\dot{\psi}(s)$ at $s = s_0$ then hold for the expressions given by (4.45), (4.42) and (4.41).